Modeling sources of the gamma-ray bursts using quasi-spherical Szekeres metrics

Andrzej Krasiński
N. Copernicus Astronomical Centre,
Polish Academy of Sciences,
*Bartycka 18, 00 716 Warszawa, Poland**
(Dated:)

In an earlier paper, using an axially symmetric Szekeres model, it was shown that infinite blueshift can appear only on those rays that intersect the symmetry axis. It was also shown that the Szekeres mass-dipole superposed on an L–T background makes any finite blueshift stronger (z becomes closer to -1) and that null geodesics with $z \approx -1$ exist also in a nonsymmetric Szekeres model. Those exemplary Szekeres spacetimes were chosen for their simplicity. In the present paper, an axially symmetric Szekeres dipole is superposed on such an L–T background that was proved, in another earlier paper, to be a promising model of a gamma-ray burst (GRB). The present model indeed makes z closer to -1 than the old one, and has the additional advantage that strong blueshifts appear only along two opposite directions, which is consistent with the hypothetical collimation of the GRBs. The model consists of a quasi-spherical Szekeres region matched into a Friedmann background. The function $t_B(r)$ is constant in the Friedmann region and has a bell-shaped hump in the Szekeres region. Since such a Szekeres island generates stronger blueshifts than an L–T island, the BB hump can be made lower. A lower hump implies a smaller observed angular radius of the GRB source. Consequently, more GRB sources can be fitted into the sky – all these facts are confirmed by numerical computations in the paper. Null geodesics reaching present GRB observers from different directions relative to the BB hump are numerically calculated, and the patterns of redshift across the image of the GRB source are shown in tables; it will be possible to compare them with observations when the resolution of the GRB-observing devices becomes sufficient for this purpose. The Szekeres models of the GRB sources also promise to explain the short durations of the GRBs and their afterglows via the effect of non-repeatability of the light paths.

PACS numbers:
Keywords:

arXiv:1704.08145v1 [gr-qc] 26 Apr 2017

I. MOTIVATION AND BACKGROUND

This paper is a continuation of Refs. [1] and [2]. In Ref. [1] it was shown that several observed properties of the gamma-ray bursts (GRBs) may be accounted for by assuming that they originate as part of the relic radiation (now seen as the cosmic microwave background, CMB), but are blueshifted rather that redshifted in consequence of the spacetime geometry at the points of their origin. Namely, the assumed spacetime model was a Friedmann background of negative spatial curvature into which several regions of Lemaître [3] – Tolman [4] (L–T) geometry with nonconstant Big Bang (BB) were matched. As has been known since long ago [5, 6], light rays emitted in an L–T model *radially*, at those points of the BB where $\mathrm{d}t_B/\mathrm{d}r \neq 0$ ($t = t_B(r)$ being the instant of the BB), will display infinite blueshift to all later observers. The matter source in the L–T models is dust, so they cannot describe epochs earlier than the last scattering, and thus in realistic examples they can generate only finite blueshifts. The problem was to arrange the profile of the BB such that it generates a blueshift between the last scattering epoch and the present time that is consistent with the lowest energy of the observed GRBs ($1+z \leq 1.689\times 10^{-5}$ [1]), and at the same time keeps the angular diameter of the GRB source sufficiently small ($\leq 0.5°$ at today's resolution [7], which is an observing error in determining the direction rather than the actual size).

The frequency range of the GRBs was successfully accounted for, but problems remained with explaining their other properties. The durations of the GRB flashes came out too long by several orders of magnitude. The model of Ref. [1] contains a parameter that *in principle* allows for controlling the durations, but insufficient numerical accuracy did not permit effective control. The angular radii of the GRB sources came out too large (1° instead of 0.5°). The sources in Ref. [1] radiated isotropically, which is in disagreement with the hypothesis that the GRBs are collimated into narrow jets.

All these defects call for improving the model. The first question to answer was: Since the ray being radial is a necessary condition for unlimited blueshift in an L–T model, can infinite blueshifts exist at all in Szekeres models [8–10] that contain L–T as a limit, but have in general no symmetry, and so no radial directions?

This question was answered in Ref. [2]. It was shown that in an axially symmetric quasi-spherical Szekeres (QSS) model, infinite blueshift can appear *only* on such rays that proceed in a constant-φ hypersurface (where φ is the azimuthal coordinate) and on those that intersect every space orthogonal to the dust flow on the symmetry axis. In an exemplary QSS model it was numerically

*Electronic address: akr@camk.edu.pl

shown that if a ray of the second type is emitted from the Big Bang where $\mathrm{d}t_B/\mathrm{d}r \neq 0$, then indeed observers see it with $z \approx -1$. Then, in an exemplary QSS model with no symmetry, it was shown by numerical calculations that two null directions exist such that rays in their vicinity have redshift profiles similar to those in a vicinity of the axial rays in the axially symmetric case. Thus, rays with strong blueshifts should exist in general QSS spacetimes and be concentrated around two directions.

In the axially symmetric case, it was also shown that a QSS deformation superposed on an L–T background extends the time of flight of the ray in the blueshift-generating region compared to the pure L–T model. Thus, using a QSS model it should be possible to make $1+z$ between the last scattering and the present time smaller than in an L–T model with the same BB profile. Consequently, to generate a given $1+z$, a lower BB hump would be needed than in an L–T spacetime, and this would have several positive consequences for a GRB model [1]. The present paper shows that this is indeed the case, although the progress is less spectacular than expected.

In Secs. II and III, the sub-family of Szekeres models employed in this paper is presented. In Sec. IV the parameters of the background Friedmann model are specified. They are different from those of the now-standard ΛCDM model [11, 12] – it was convenient to keep them the same as in the earlier-discussed models. In Sec. V, the equations of null geodesics in the QSS model considered here are presented. In Sec. VI, basic properties of redshift are described, and the conditions for $z=-1$ in an axially symmetric QSS are spelled out. In Sec. VII, the equation of the Extremum Redshift Surface (ERS) is derived.[1] On this surface, z calculated along axial rays has maxima or minima. In Sec. VIII, the specific QSS/Friedmann model used in this paper is introduced, and its numerical parameters are adapted to modelling the GRBs of lowest frequency. In Sec. IX, the equations of rays reaching the present GRB-observers are numerically integrated and the solutions are displayed. The observers are placed in three directions with respect to the QSS region: (I) – in prolongation of the dipole minimum of the Szekeres region, (II) – in prolongation of the dipole maximum, and (III) – in prolongation of the dipole equator of the boundary of the Szekeres region. For each observer, the resulting redshift profiles *across* the image of the radiation source are presented in tables. In Sec. X, redshift profiles *along* the nonaxial rays reaching Observer I are displayed to show that analogues of the ERS exist also along nonaxial directions. In Section XI it is estimated how many such GRB model-sources could be simultaneously fitted into the celestial sphere, and the resulting number ($\approx 11,000$) is consistent with the available information on the number of observed GRBs. Possible further improvements of the model are discussed in Sec. XII. Section XIII contains the summary and conclusions. In particular it discusses the prospects of observational verification of this and other models and of explaining the short durations of the GRBs and their afterglows via the effect of non-repeatability of the light paths discussed in Refs. [13] and [14].

[1] Sections II, IV, V and VII are partly copied from Ref. [2].

II. THE QUASISPHERICAL SZEKERES (QSS) SPACETIMES

The metric of the QSS spacetimes is [8–10, 15]

$$\mathrm{d}s^2 = \mathrm{d}t^2 - \frac{\left(\Phi_{,r} - \Phi\mathcal{E}_{,r}/\mathcal{E}\right)^2}{1+2E(r)}\mathrm{d}r^2 - \left(\frac{\Phi}{\mathcal{E}}\right)^2\left(\mathrm{d}x^2+\mathrm{d}y^2\right), \tag{2.1}$$

where

$$\mathcal{E} \stackrel{\mathrm{def}}{=} \frac{S}{2}\left[\left(\frac{x-P}{S}\right)^2 + \left(\frac{y-Q}{S}\right)^2 + 1\right], \tag{2.2}$$

$P(r)$, $Q(r)$, $S(r)$ and $E(r)$ being arbitrary functions such that $S \neq 0$ and $E \geq -1/2$ at all r.

The source in the Einstein equations is dust ($p=0$) with the velocity field $u^\alpha = \delta_0{}^\alpha$. The surfaces of constant t and r are nonconcentric spheres, and (x,y) are the stereographic coordinates on each sphere. At a fixed r, they are related to the spherical coordinates by

$$\begin{aligned} x &= P + S\cot(\vartheta/2)\cos\varphi, \\ y &= Q + S\cot(\vartheta/2)\sin\varphi. \end{aligned} \tag{2.3}$$

The functions (P,Q,S) determine the centres of the spheres in the spaces of constant t (see illustrations in Ref. [2]). Because of the non-concentricity, the QSS spacetimes in general have no symmetry [16].

With $\Lambda = 0$ assumed, $\Phi(t,r)$ obeys

$$\Phi_{,t}{}^2 = 2E(r) + \frac{2M(r)}{\Phi}, \tag{2.4}$$

where $M(r)$ is an arbitrary function. We will consider only models with $E>0$, and then

$$\begin{aligned} \Phi(t,r) &= \frac{M}{2E}(\cosh\eta - 1), \\ \sinh\eta - \eta &= \frac{(2E)^{3/2}}{M}\left[t - t_B(r)\right], \end{aligned} \tag{2.5}$$

where $t_B(r)$ is one more arbitrary function; $t = t_B(r)$ is the BB time, at which $\Phi(t_B,r)=0$. We assume $\Phi_{,t}>0$ (the Universe is expanding).

The mass density implied by (2.1) is

$$\kappa\rho = \frac{2\left(M_{,r} - 3M\mathcal{E}_{,r}/\mathcal{E}\right)}{\Phi^2\left(\Phi_{,r} - \Phi\mathcal{E}_{,r}/\mathcal{E}\right)}, \quad \kappa \stackrel{\mathrm{def}}{=} \frac{8\pi G}{c^2}. \tag{2.6}$$

This density distribution is a mass-dipole superposed on a spherically symmetric monopole [9, 17]. The dipole,

generated by $\mathcal{E}_{,r}/\mathcal{E}$, vanishes where $\mathcal{E}_{,r}=0$. The density is minimum where $\mathcal{E}_{,r}/\mathcal{E}$ is maximum and vice versa [18].

The arbitrary functions must be such that $0<\rho<\infty$ at $t>t_B(r)$. The conditions that ensure this are [18]:

$$\frac{M_{,r}}{3M} \geq \frac{\sqrt{(S_{,r})^2+(P_{,r})^2+(Q_{,r})^2}}{S} \qquad \forall\ r, \quad (2.7)$$

$$\frac{E_{,r}}{2E} > \frac{\sqrt{(S_{,r})^2+(P_{,r})^2+(Q_{,r})^2}}{S} \qquad \forall\ r. \quad (2.8)$$

These inequalities imply [18]

$$\frac{M_{,r}}{3M} \geq \frac{\mathcal{E}_{,r}}{\mathcal{E}}, \qquad \frac{E_{,r}}{2E} > \frac{\mathcal{E}_{,r}}{\mathcal{E}} \qquad \forall\ r. \quad (2.9)$$

The extrema of $\mathcal{E}_{,r}/\mathcal{E}$ with respect to (x,y) are [18]

$$\left.\frac{\mathcal{E}_{,r}}{\mathcal{E}}\right|_{\text{extreme}} = \pm\frac{\sqrt{(S_{,r})^2+(P_{,r})^2+(Q_{,r})^2}}{S}, \quad (2.10)$$

with + corresponding to maximum and − to minimum. In the following, we will call these two loci "dipole maximum" and "dipole minimum", respectively.

The L–T models are contained in the QSS models as the limit of constant (P,Q,S). Then the constant-(t,r) spheres become concentric, and the spacetime becomes spherically symmetric. The Friedmann limit is obtained when $E/M^{2/3}$ and t_B are constant, with arbitrary (P,Q,S) (in this limit, (P,Q,S) can be made constant by a coordinate transformation). A QSS spacetime can be matched to a Friedmann spacetime across an $r=$ constant hypersurface.

Because of $p=0$, the QSS models can describe the past evolution of the Universe no further than to the last scattering hypersurface (LSH). See Sec. VIII for information on how to determine it in our model.

III. THE QSS MODELS CONSIDERED IN THIS PAPER

We will consider such QSS spacetimes whose L–T limit is Model 2 of Ref. [1]. The r-coordinate is chosen so that

$$M = M_0 r^3, \quad (3.1)$$

and $M_0=1$ (kept in formulae for dimensional clarity) [19]. From this point on, the r-coordinate is unique. The function $E(r)$, assumed in the form

$$2E/r^2 \stackrel{\text{def}}{=} -k = 0.4, \quad (3.2)$$

is the same as in the background Friedmann model.

The units used in numerical calculations were introduced and justified in Ref. [20]. Taking [21]

$$1\text{ pc} = 3.086\times10^{13}\text{ km}, \quad 1\text{ y} = 3.156\times10^{7}\text{ s}, \quad (3.3)$$

the numerical length unit (NLU) and the numerical time unit (NTU) are defined as follows:

$$\begin{aligned} 1\text{ NTU} &= 1\text{ NLU} = 9.8\times10^{10}\text{ y} \\ &= 3\times10^{4}\text{ Mpc}. \end{aligned} \quad (3.4)$$

The BB profile belongs to the same 5-parameter family as in Ref. [1], see Fig. 1. It consists of two curved arcs and of a straight line segment joining them. The upper-left arc, shown in thicker line, is a segment of the curve

$$\frac{r^6}{{B_1}^6} + \frac{(t-t_{\text{Bf}}-A_0)^6}{{B_0}^6} = 1, \quad (3.5)$$

where

$$t_{\text{Bf}} = -0.13945554689046649\,\text{NTU} \approx -13.67\times10^9\text{ years}; \quad (3.6)$$

see Sec. IV for comments on this value. The lower-right arc (also shown in thicker line) is a segment of the ellipse

$$\frac{(r-B_1-A_1)^2}{{A_1}^2} + \frac{(t-t_{\text{Bf}}-A_0)^2}{{A_0}^2} = 1. \quad (3.7)$$

The straight segment[2] passes through the point $(r,t)=(B_1, t_{\text{Bf}}+A_0)$ where the full curves (shown in dotted lines) would meet; its slope is determined by x_0.

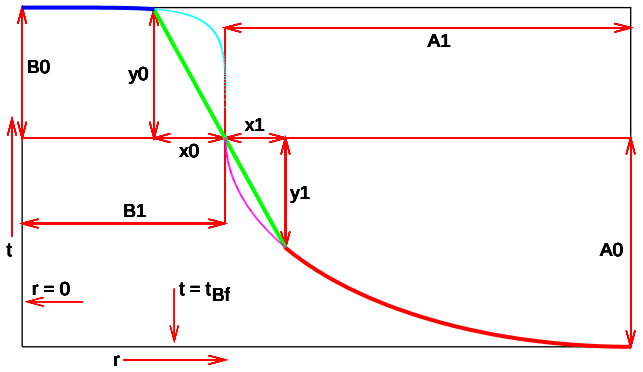

FIG. 1: Parameters of the bang-time profile in the quasi-spherical Szekeres region; see text for explanation.

The free parameters are A_0, A_1, B_0, B_1 and x_0. Figure 1 does not show the values used in numerical calculations; in particular x_0 and A_1 are greatly exaggerated. The actual values are [1]

$$\begin{pmatrix} A_0 \\ B_0 \\ A_1 \\ B_1 \\ x_0 \end{pmatrix} = \begin{pmatrix} 0.000026\text{ NTU} \\ 0.0001\text{ NTU} \\ 1\times10^{-10} \\ 0.015 \\ 2\times10^{-13} \end{pmatrix} \quad (3.8)$$

(A_1, B_1 and x_0 are dimensionless). This profile will be the starting point for modifications.

The QSS model used here is axially symmetric, with $P(r)=Q(r)=0$ and $S(r)$ the same as in Ref. [2]:

$$S = \sqrt{a^2+r^2}, \quad (3.9)$$

[2] It was introduced to keep $\mathrm{d}t_B/\mathrm{d}r$ finite everywhere; it is invisible in some of the figures because x_0 is extremely small.

where $a > 0$ is a constant, and so

$$\mathcal{E} = \frac{1}{2S}\ \left(x^2 + y^2 + S^2\right); \tag{3.10}$$

This $S(r)$ obeys (2.7) and (2.8), which, using (3.1) and (3.2), both reduce to

$$1/r > S_{,r}\,/S. \tag{3.11}$$

The equation of the dipole "equator" $\mathcal{E}_{,r} = 0$ is

$$x^2 + y^2 = S^2, \tag{3.12}$$

the axis of symmetry is $x = y = 0$, and the extrema of the dipole are, from (2.10)

$$\left.\frac{\mathcal{E}_{,r}}{\mathcal{E}}\right|_{\text{extreme}} = \pm\frac{S_{,r}}{S}. \tag{3.13}$$

At $r > r_b$, where

$$r_b = A_1 + B_1, \tag{3.14}$$

the BB profile becomes flat, and the geometry of the model becomes Friedmannian. See Sec. V for remarks on the choice of coordinates in that region.

IV. THE BACKGROUND MODEL

Our Friedmann background is defined by:

$$\Lambda = 0, \tag{4.1}$$

$$k = -0.4, \tag{4.2}$$

$$t_B \overset{\text{def}}{=} t_{\text{Bf}} = -0.13945554689046649\ \text{NTU} \approx -13.67 \times 10^9\ \text{years}, \tag{4.3}$$

where k is the curvature index and t_B is the BB time; $t = 0$ is the present time. The t_{Bf} is the asymptotic value of the function $t_B(r)$ in the L–T model that mimicked accelerating expansion [19] (first presented in Ref. [20]). This differs by $\sim 1.6\%$ from $(-T)$, where T is the age of the Universe given by the Planck satellite team [11]

$$T = 13.819 \times 10^9\ \text{y} = 0.141\ \text{NTU}. \tag{4.4}$$

The density at the last scattering time is [1]

$$\kappa\rho_{\text{LS}} = 56.1294161975316 \times 10^9\ (\text{NLU})^{-2}. \tag{4.5}$$

This value follows from the model of the cosmological recombination process [22–24] and is independent of the after-recombination model. With (4.1) – (4.3), ρ_{LS} implies the redshift relative to the present time

$$1 + z^{\text{b}}_{\text{LS}} = 952.611615159. \tag{4.6}$$

This differs by $\sim 12.7\%$ from the ΛCDM value [11, 12]

$$z_{\text{LS}} = 1090. \tag{4.7}$$

The present temperature of the CMB radiation is directly measured, so if (4.6) were taken for real, it would imply that the temperature of the background radiation at emission was $\sim$ 3380 K instead of $\sim$ 3000 K dictated by current knowledge. To bring our model to agreement with these data, laborious re-calculations would be required. Since our model needs improvements anyway, we will rather stick to (4.1) – (4.3), to be able to compare the present results with the earlier ones.

V. NULL GEODESICS IN THE AXIALLY SYMMETRIC QSS SPACETIMES

In an axially symmetric QSS metric, the (x, y)-coordinates can be chosen such that $P = Q = 0$; then $(x, y) = (0, 0)$ is the symmetry axis and a family of axial null geodesics exists along which $x = y = 0$ [25, 26]. However, the loci $x = \infty$ and $y = \infty$ are coordinate singularities (they represent the pole of the stereographic projection of a sphere), and the numerical integration of nonaxial geodesics breaks down on crossing those sets. Therefore, we introduce the new coordinates (ϑ, φ) by

$$x = S_b \cot(\vartheta/2)\cos\varphi, \qquad y = S_b \cot(\vartheta/2)\sin\varphi, \tag{5.1}$$

where

$$S_b \overset{\text{def}}{=} S(r_b) = \sqrt{a^2 + {r_b}^2} \tag{5.2}$$

is the value of S at the Szekeres/Friedmann boundary. This changes (2.1) and (2.2) to

$$\mathrm{d}s^2 = \mathrm{d}t^2 - \frac{\mathcal{N}^2\mathrm{d}r^2}{1 + 2E(r)} - \left(\frac{\Phi}{\mathcal{F}}\right)^2 \left(\mathrm{d}\vartheta^2 + \sin^2\vartheta\mathrm{d}\varphi^2\right), \tag{5.3}$$

$$\mathcal{F} = \frac{S_b}{2S}\ (1 + \cos\vartheta) + \frac{S}{2S_b}\ (1 - \cos\vartheta), \tag{5.4}$$

where

$$\mathcal{N} \overset{\text{def}}{=} \Phi_{,r} - \Phi\mathcal{F}_{,r}\,/\mathcal{F}. \tag{5.5}$$

The dipole equator $\mathcal{F}_{,r} = 0$ is now at $\cot(\vartheta_{\text{eq}}/2) = S/S_b$ (so $\vartheta_{\text{eq}} = \pi/2$ in the Friedmann region, including the QSS boundary). On the boundary sphere $r = r_b$ we have $\mathcal{F} = 1$ and (ϑ, φ) become the spherical coordinates with the origin at $r = 0$. Along a geodesic we denote

$$\left(k^t, k^r, k^\vartheta, k^\varphi\right) \overset{\text{def}}{=} \frac{\mathrm{d}(t, r, \vartheta, \varphi)}{\mathrm{d}\lambda}, \tag{5.6}$$

where λ is an affine parameter. In these coordinates, the geodesic equations for (5.3) – (5.4) are

$$\frac{\mathrm{d}k^t}{\mathrm{d}\lambda}\ +\ \frac{\mathcal{N}\mathcal{N}_{,t}}{1 + 2E}\,(k^r)^2 + \frac{\Phi\Phi_{,t}}{\mathcal{F}^2}\left[\left(k^\vartheta\right)^2 + \sin^2\vartheta\,(k^\varphi)^2\right] = 0, \tag{5.7}$$

$$\begin{aligned}\frac{\mathrm{d}k^r}{\mathrm{d}\lambda} &+ 2\frac{\mathcal{N}_{,t}}{\mathcal{N}}k^t k^r \\ &+ \left(\frac{\mathcal{N}_{,r}}{\mathcal{N}} - \frac{E_{,r}}{1+2E}\right)(k^r)^2 + 2\frac{S_{,r}\sin\vartheta\Phi}{S\mathcal{F}^2\mathcal{N}}\ k^r k^\vartheta \\ &- \frac{\Phi(1+2E)}{\mathcal{F}^2\mathcal{N}}\left[\left(k^\vartheta\right)^2 + \sin^2\vartheta\,(k^\varphi)^2\right] = 0, \quad (5.8)\\ \frac{\mathrm{d}k^\vartheta}{\mathrm{d}\lambda} &+ 2\frac{\Phi_{,t}}{\Phi}k^t k^\vartheta - \frac{S_{,r}\sin\vartheta\mathcal{N}}{S\Phi(1+2E)}\ (k^r)^2 + 2\frac{\mathcal{N}}{\Phi}k^r k^\vartheta \\ &+ \frac{\mathcal{F}_{,\vartheta}}{\mathcal{F}}\ \left[-\left(k^\vartheta\right)^2 + \sin^2\vartheta\,(k^\varphi)^2\right] \\ &- \cos\vartheta\sin\vartheta\,(k^\varphi)^2 = 0, \quad (5.9)\\ \frac{\mathrm{d}k^\varphi}{\mathrm{d}\lambda} &+ 2\frac{\Phi_{,t}}{\Phi}k^t k^\varphi + 2\frac{\mathcal{N}}{\Phi}k^r k^\varphi \\ &+ 2\left[\frac{\cos\vartheta}{\sin\vartheta} - \frac{\mathcal{F}_{,\vartheta}}{\mathcal{F}}\right]k^\vartheta k^\varphi = 0. \quad (5.10)\end{aligned}$$

The geodesics determined by (5.7) – (5.10) are null when

$$\left(k^t\right)^2 - \frac{\mathcal{N}^2(k^r)^2}{1+2E(r)} - \left(\frac{\Phi}{\mathcal{F}}\right)^2\left[\left(k^\vartheta\right)^2 + \sin^2\vartheta\,(k^\varphi)^2\right] = 0. \quad (5.11)$$

Let the subscript o refer to the observation point. On past-directed rays $k^t < 0$ and the affine parameter along each one of them can be chosen such that

$$k^t_o = -1. \quad (5.12)$$

Then, from (5.11) we have

$$\left(k^\vartheta_o\right)^2 + \sin^2\vartheta\,(k^\varphi_o)^2 \le \left(\frac{\mathcal{F}_o}{\Phi_o}\right)^2; \quad (5.13)$$

the equality occurs when the ray is tangent to a hypersurface of constant r at the observation event, $k^r_o = 0$.

On the boundary $r = r_b$ between the QSS and Friedmann regions the coordinates on both sides must coincide. Thus, for the Friedmann region one must use the metric (5.3) with $t_B = t_{\mathrm{Bf}}$ given by (3.6) (E has the Friedmann form everywhere in consequence of (3.2)). As stated in Sec. II, the metric then becomes Friedmann with no further limitation on S. However, with S being of the general form (3.9), the r-coordinate in the Friedmann region would be different from the one used in Ref. [1]. Therefore, for correspondence, in the Friedmann region we choose the coordinates so that

$$S = \sqrt{a^2 + {r_b}^2} = S_b. \quad (5.14)$$

Then, $\mathcal{F} = 1$ and (ϑ, φ) are the spherical coordinates throughout the Friedmann region.

To calculate k^r on nonradial null geodesics, (5.11) will be used, which is insensitive to the sign of k^r. Therefore, a numerical program for integrating the set {(5.7), (5.9) – (5.11)} will have to change the sign of k^r at each point where k^r reaches zero.

In the following, the coordinate labels will be

$$\left(x^0, x^1, x^2, x^3\right) = (t, r, \vartheta, \varphi). \quad (5.15)$$

Note that $k^\varphi \equiv 0$ is a solution of (5.10) while $\vartheta \equiv 0$ and $\vartheta \equiv \pi$ (both implying $k^\vartheta \equiv 0$) are solutions of (5.9). Rays with these properties intersect every space of constant t on the symmetry axis; they will be called axial rays. However, there exist no null geodesics on which $k^\varphi \equiv 0$ and ϑ has any constant value other than 0 or π. This follows from (5.9): Suppose $k^\varphi \equiv 0$ everywhere and $k^\vartheta = 0$ at a point. Then, if $\sin\vartheta \neq 0$, the third term in (5.9) will be nonzero (because $|S\Phi(1+2E)| < \infty$, $S_{,r} \neq 0$ from (3.9), $\mathcal{N} \neq 0$ from no-shell-crossing conditions [18] and $k^r \neq 0$ from (5.11)), and so $\mathrm{d}k^\vartheta/\mathrm{d}\lambda \neq 0$. Consequently, in the axially symmetric case the only analogues of radial directions are $\vartheta = 0$ and $\vartheta = \pi$, with any constant φ. The fact reported under (6.4) below is consistent with this.

The coefficient $1/\Phi$ in front of $(k^r)^2$ and of k^r in (5.9) and (5.10) becomes infinite at $r = 0$, where $\Phi = 0$ [1], and $\Phi_{,t}/\Phi$ becomes indeterminate. See Ref. [2] for a discussion of this; all the suspicious-looking terms are in fact finite there. In the present paper the only geodesics running through $r = 0$ will be the axial ones, on which (5.9) and (5.10) are obeyed identically.

VI. THE REDSHIFT IN AXIALLY SYMMETRIC QSS SPACETIMES

Along a ray emitted at P_e and observed at P_o we have

$$1 + z = \frac{(u_\alpha k^\alpha)_e}{(u_\alpha k^\alpha)_o}, \quad (6.1)$$

where u_α are the four-velocities of the emitter and of the observer, and k^α is the affinely parametrised tangent vector field to the ray [27]. In our case, both the emitter and the observer will be assumed to comove with the cosmic matter, so $u_\alpha = \delta^0{}_\alpha$, and then (6.1) simplifies to $1 + z = {k_e}^t/{k_o}^t$. A further simplification results when the affine parameter is rescaled so that (5.12) holds; then

$$1 + z = -{k_e}^t. \quad (6.2)$$

Equation (5.10) has the first integral:

$$k^\varphi \sin^2\vartheta\Phi^2/\mathcal{F}^2 = J_0, \quad (6.3)$$

where J_0 is constant along each geodesic. When (6.3) is substituted in (5.11), the following results:

$$(k^t)^2 = \frac{\mathcal{N}^2(k^r)^2}{1+2E} + \left(\frac{\Phi}{\mathcal{F}}\right)^2\left(k^\vartheta\right)^2 + \left(\frac{J_0\mathcal{F}}{\sin\vartheta\Phi}\right)^2. \quad (6.4)$$

At the observation/emission point, (5.12)/(6.2), respectively, apply. Equations (6.4) and (6.2) show that for rays emitted at the BB, where $\Phi = 0$, the observed redshift is infinite when $J_0 \neq 0$. A necessary condition for infinite blueshift ($1 + z_o = 0$) is thus $J_0 = 0$, so

(a) either $k^\varphi = 0$, i.e. the ray proceeds within the hypersurface of constant φ,

(b) or $\vartheta = 0$ or $\vartheta = \pi$ along the ray (Eq. (6.3) implies that $J_0/\sin\vartheta \to 0$ when $\vartheta \to 0, \pi$.).

The second condition appears to be also sufficient, but so far this has been demonstrated only numerically in concrete examples of QSS models ([2] and Sec. VIII here).

The following property of z that follows from (6.1) is useful in numerical calculations. Consider a ray proceeding from event P_1 to P_2 and then from P_2 to P_3. Denote the redshifts acquired in the intervals $[P_1, P_2]$, $[P_2, P_3]$ and $[P_1, P_3]$ by z_{12}, z_{23} and z_{13}, respectively. Then

$$1 + z_{13} = (1 + z_{12})\,(1 + z_{23})\,. \tag{6.5}$$

In particular, for a ray proceeding to the past from P_1 to P_2, and then back to the future from P_2 to P_1:

$$1 + z_{12} = \frac{1}{1 + z_{21}}. \tag{6.6}$$

These properties allow one to split the numerical calculation of z into segments and then combine the results.

VII. THE EXTREMUM REDSHIFT SURFACE

Consider a null geodesic that stays in the surface $\{\vartheta, \varphi\} = \{\pi, \text{constant}\}$; it obeys (5.9) and (5.10) identically. On it, $k^r \neq 0$ at all points because with $k^\vartheta = k^\varphi = 0$ the geodesic would be timelike wherever $k^r = 0$. Assume the geodesic is past-directed and has its initial point at $r = 0$. Thus, r has to increase along it and can be used as a parameter. Using (6.2) and changing the parameter to r, we obtain from (5.7)

$$\frac{\mathrm{d}z}{\mathrm{d}r} = \frac{\mathcal{N}\mathcal{N}_{,t}}{1 + 2E}\; k^r. \tag{7.1}$$

Since $\mathcal{N} \neq 0$ from no-shell-crossing conditions [18] and $k^r > 0$, the extrema of z on such a geodesic occur where

$$\mathcal{N}_{,t} \equiv \Phi_{,tr} - \Phi_{,t}\, \mathcal{F}_{,r}\, / \mathcal{F} = 0. \tag{7.2}$$

In deriving (7.2), $\vartheta = \pi$ was assumed. Thus, the set in spacetime defined by (7.2) is 2-dimensional; it is the Extremum Redshift Surface (ERS) [2].

From (2.4) and (3.2) we obtain

$$\Phi_{,t} \;=\; r\sqrt{\frac{2M_0 r}{\Phi} - k}, \tag{7.3}$$

$$\Phi_{,tr} \;=\; \sqrt{\frac{2M_0 r}{\Phi} - k} + \frac{M_0 r^3}{\Phi^2}\; t_{B,r}. \tag{7.4}$$

Using (7.3), (7.4) and (5.4) with $\vartheta = \pi$, Eq. (7.2) becomes

$$\sqrt{\frac{2M_0 r}{\Phi} - k}\left(1 - r\frac{S_{,r}}{S}\right) = -\frac{M_0 r^3}{\Phi^2}\; t_{B,r}. \tag{7.5}$$

To avoid shell crossings, $t_{B,r} < 0$ must hold at all $r > 0$ [18], [10],[3] so the right-hand side of (7.5) is non-negative. The left-hand side is positive with S given by (3.9). Using (2.5) for Φ, remembering that $k < 0$ and denoting

$$\chi \stackrel{\text{def}}{=} \sinh^2(\eta/2) \tag{7.6}$$

we obtain from (7.5)

$$\chi^4 + \chi^3 = -k^3 \left[\frac{r t_{B,r}}{4M_0\,(1 - rS_{,r}\,/S)}\right]^2. \tag{7.7}$$

With $k < 0$, (7.7) is solvable for χ at any r, since its left-hand side is independent of r and can vary from 0 to $+\infty$ while the right-hand side is non-negative.

Note that where $t_{B,r} = 0$, Eqs. (7.7) and (7.6) imply $\chi = \eta = 0$, i.e. at those points the ERS is tangent to the BB. Note also that the ERS is tangent to the BB at $r = 0$ unless $\mathrm{d}t_B/\mathrm{d}r \underset{r\to 0}{\longrightarrow} \infty$. This would imply $\mathrm{d}\rho/\mathrm{d}r \underset{r\to 0}{\longrightarrow} \infty$, an infinitely thin peak in density at $r = 0$ – an unusual configuration, but *not a curvature singularity* [28]. The model considered here will have $t_{B,r} = 0$ at $r = 0$.

In the limit $S_{,r} = 0$, (7.7) reproduces the equation of the Extremum Redshift *Hyper*surface (ERH) of Ref. [19].

Equation (7.7) was derived for null geodesics proceeding along $\vartheta = \pi$, where the dipole contribution to mass density is maximum, $\mathcal{F}_{,r}\,/\mathcal{F} = S_{,r}\,/S > 0$. Note that with S given by (3.9) we have

$$F_1 \stackrel{\text{def}}{=} 1/\,(1 - rS_{,r}\,/S) = (r/a)^2 + 1 > 1, \tag{7.8}$$

so, at a given r, the ERS has a greater η (and so a greater $t - t_B$) than the corresponding ERH of the L–T model. Also, the extrema of z along the dipole maximum occur at a greater χ (and thus greater $t - t_B$) when a is smaller. This will be illustrated by Fig. 2 in the next section.

Conversely, for a ray proceeding along the dipole minimum axis (where $\vartheta = 0$), the factor F_1 is replaced by

$$F_2 \stackrel{\text{def}}{=} 1/\,(1 + rS_{,r}\,/S) = \frac{a^2 + r^2}{a^2 + 2r^2} < 1, \tag{7.9}$$

and so the ERS has a *smaller* $t - t_B$ than the ERH in L–T. Also here, a smaller a has a more pronounced effect.

Extrema of redshift exist also along other directions than $\vartheta = 0$ and $\vartheta = \pi$, as will be demonstrated by numerical examples further on in in this paper, but a general equation defining their loci remains to be derived.

VIII. A GENERALISED MODEL 2 OF REF. [1]

Along each past-directed null geodesic, the mass density is calculated using (2.5) – (2.6). As explained in Sec. IV, in any model the density at the LSH must be the same as in (4.5). So, the instant of crossing the LSH is that where the density becomes equal to (4.5).

The starting point for this paper was Model 2 of Ref. [1], whose functions $M(r)$, $E(r)$ and $t_B(r)$ are given by

[3] Refs. [18] and [10] did not spell out the condition $r > 0$ in deriving the no-shell-crossing conditions, but it is implicitly there.

(3.1), (3.2) and (3.5) – (3.8). In that model, the strongest blueshift between the LSH and the present epoch was

$$1 + z_{\rm maxb} = 1.36167578 \times 10^{-5}. \qquad (8.1)$$

It was calculated by the rule (6.5). The first factor,

$$1 + z_{\rm ols2} = 1.07858890707746014 \times 10^{-7}, \qquad (8.2)$$

was the blueshift between the LSH and $r = 0$, achieved on a path that will be called "ray A". The second factor,

$$1 + z_{\rm po2} = 126.246039921. \qquad (8.3)$$

was the redshift between $r = 0$ and the present epoch achieved on a path going off from the same initial point as ray A, but to the future; it will be called "ray B". [4]

For this paper, the L–T model with parameters given by (3.8) was taken as the starting point. On it, axially symmetric QSS deformations given by $P = Q = 0$, (3.9) and (3.10) were superposed, and numerical experiments with rays proceeding along $\vartheta = \pi$ were done to improve on (8.2) as much as possible. As explained at the end of Sec. VII, smaller a increases the region under the ERS. So, with the parameters of (3.8) unchanged at first, a^2 was gradually decreased from 10 through 1, 1/10, 10^{-2}, 10^{-3} to 10^{-4}. For each a the quantity

$$t(0) - t_B(0) \stackrel{\rm def}{=} \Delta t_c \qquad (8.4)$$

was chosen such as to obtain a minimum $1 + z$ between the LSH and $r = 0$. This led to smaller $1+z$ on ray A only down to $a^2 = 0.001$. With a^2 still smaller, the ray either flew over the BB hump and acquired a large $z > 0$ at the LSH or dipped under the LSH with a small $z > 0$. No intermediate value of Δt_c led to $z < 0$ (but this discontinuity could perhaps be overcome with greater numerical precision). The best result achieved with $a^2 = 0.001$ was $1 + z_2 = 8.87933914173189009 \times 10^{-8}$.

In the next experiments, the slope of the straight segment of the BB profile was gradually decreased, i.e x_0 was increased from 2×10^{-13} through 1×10^{-12} to 1×10^{-11}, with the other parameters unchanged. For each value of x_0, the Δt_c leading to the smallest $1 + z$ was determined. The best result achieved at this stage was

$$1 + z_1 = 6.74014204449235876 \times 10^{-8}. \qquad (8.5)$$

Varying A_1, B_1, B_0, and lowering the degree of (3.5) to 4 and to 2, led to nothing better than (8.5). So, this will be taken as the best improvement over the L–T model achieved using an axially symmetric QSS deformation.

Figure 2 shows ray A, with $1+z_1$ given by (8.5), and the corresponding ERS and BB profiles. (The BB profile of Model 2 from Ref. [1] is, at this scale, indistinguishable from the one shown). Two other profiles illustrate the influence of a on the ERS. Curve 1 is the ERH profile of the L–T Model 2 from Ref. [1], and Curve 2 is the ERS profile with $a^2 = 10^{-5}$. As stated above, smaller a gives more space under the ERS, but when too small it creates a discontinuity in z that prevents $z < 0$ altogether.

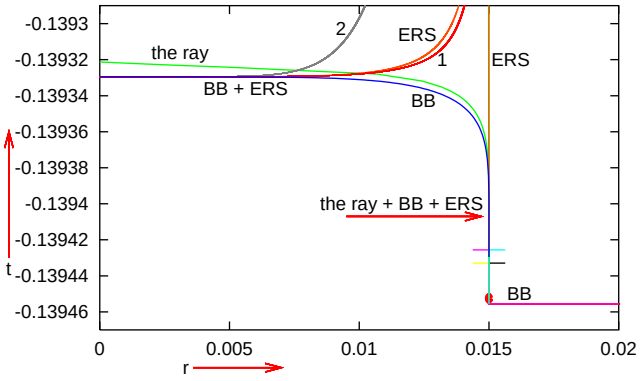

FIG. 2: The Big Bang profile and the axial ray with the smallest $1 + z$ in the Szekeres model. The dot shows where the ray hits the LSH. See text for more explanation.

The ERS profile has two branches on each side of $r = 0$, so some rays will intersect it four times and z along them will have two local maxima and two local minima. Examples will appear later in this paper.

On ray B, $1 + z$ calculated following the ray was

$$1 + z_{1\ \rm up} = 6.39228356761256666 \times 10^{-3}. \qquad (8.6)$$

Thus, total $(1 + z)$ between LSH and now is

$$1 + z_2 = \frac{1 + z_1}{1 + z_{1\ \rm up}} = 1.05441849899 \times 10^{-5} \quad . \qquad (8.7)$$

This fits the lowest-frequency GRBs, for which [1]

$$1 + z_{\rm max} \approx 1.689 \times 10^{-5}, \qquad (8.8)$$

with a wider margin than (8.1), so the BB hump could now be lowered to yield $(1 + z)$ closer to (8.8).

The easiest way to do this was to decrease B_0 (see Fig. 1) and then fine-tune Δt_c to make $(1 + z_{\rm ols})$ on ray A as small as possible ($1 + z_{\rm ols}$ gets larger when B_0 gets smaller, so there is a limit on decreasing B_0). The B_0 that allowed sufficiently small $(1 + z)_{\rm ols}$ was

$$B_0 = 0.000091, \qquad (8.9)$$

and the smallest $1 + z$ on ray A was

$$1 + z_{\rm ols3} = 1.11939135405414447 \times 10^{-7}. \qquad (8.10)$$

The step in the affine parameter λ on rays sent to the future from $r = 0$ was chosen the same as in Ref. [1], $\Delta\lambda = 4 \times 10^{-7}$. For ray B corresponding to ray A of

[4] This way of calculating $1 + z$ allowed one to avoid multiple calculations between $r = 0$ and now, which takes a long time. Only the first factor had to be calculated many times.

(8.10) (proceeding along the dipole minimum), the $1+z$ between $r=0$ and the present epoch was

$$1+z_{3\ \rm up}=7.20622328938758105\times10^{-3}, \tag{8.11}$$

so $(1+z)$ between LSH and now along rays A and B was[5]

$$1+z_3=\frac{1+z_{\rm ols3}}{1+z_{3\ \rm up}}=1.553\times10^{-5}, \tag{8.12}$$

and the present observer came out to be at

$$r=r_{\rm obs}=0.88918723168057401. \tag{8.13}$$

This is larger than $r_{\rm O2}=0.88705643159726955$ in Model 2 of Ref. [1]. Thus, a Szekeres deformation superposed on an L–T model results in moving the observer further away from the GRB source, which leads to a smaller angular diameter of the source seen in the sky; see Sec. IX.

Rays A and B referred to above had

$$\Delta t_c=0.00000863099500\ {\rm NTU}. \tag{8.14}$$

The corresponding results for rays propagating in the opposite direction, i.e. along the dipole minimum between the LSH and $r=0$ (ray C), and along the dipole maximum between $r=0$ and the observer (ray D), are as follows. The best value of $1+z$ on ray C was

$$1+z_{1\ \rm dip\ min}=1.73185662921682137\times10^{-7}, \tag{8.15}$$

achieved with

$$\Delta t_c=0.00000981550000\ {\rm NTU}. \tag{8.16}$$

With this Δt_c, the $1+z$ calculated toward the future along the dipole maximum was

$$1+z_{2\ \rm dmax\ up}=7.26948511585012724\times10^{-3}. \tag{8.17}$$

So, the $1+z$ between the LSH and the present time was

$$1+z_4=\frac{1+z_{1\ \rm dip\ min}}{1+z_{2\ \rm dmax\ up}}=2.382\times10^{-5}. \tag{8.18}$$

The present time was reached by the ray at

$$\widetilde{r}_{\rm obs}=0.88935629118490100. \tag{8.19}$$

Thus, on this ray $1+z$ and $r_{\rm obs}$ are larger. (The small difference in $r_{\rm obs}$ might be caused by numerical errors).

In each case the numerical calculation overshot the present time. For the ray that produced (8.11) and (8.13), the value of t at the endpoint was

$$t_{\rm end\ 1}=2.05240714619817272\times10^{-9}\ {\rm NTU}, \tag{8.20}$$

and for the ray that produced (8.17) and (8.19) it was

$$t_{\rm end\ 2}=9.65282969667925857\times10^{-10}\ {\rm NTU}. \tag{8.21}$$

[5] The limit (8.8) would allow a still larger $1+z_3$, i.e., a smaller B_0 and larger $r_{\rm obs}$, but (8.12) is sufficient to illustrate the influence of the Szekeres deformation on the L–T results.

IX. NONAXIAL PLANE RAYS

So far, rays crossing the symmetry axis of the $t=$ constant spaces in the metric (5.3) – (5.4) were considered. Now, we will consider nonaxial rays (ϑ will no longer be 0 or π all along the ray) propagating in a hypersurface of constant φ, in which thus $k^\varphi=0$. By (6.3), $J_0=0$ along such rays and they obey (5.10) identically. Because of axial symmetry of the model, the image will be the same for every φ.

We will consider pencils of rays flying through the vicinity of the BB hump shown in Fig. 2 and reaching the present observer situated in three locations:

Observer I: At

$$(t,r,\vartheta)_{\rm I}=(t_{\rm end\ 1},r_{\rm obs},0), \tag{9.1}$$

with $r_{\rm obs}$ given by (8.13). This is the endpoint of ray B of Sec. VIII.

Observer II: At

$$(t,r,\vartheta)_{\rm II}=(t_{\rm end\ 2},\widetilde{r}_{\rm obs},\pi), \tag{9.2}$$

with $\widetilde{r}_{\rm obs}$ given by (8.19). This is the endpoint of ray D of Sec. VIII.

Observer III: At

$$(t,r,\vartheta)_{\rm III}=(0,r_p,\pi/2),\quad \text{where}\quad r_p=(r_{\rm obs}+\widetilde{r}_{\rm obs})/2. \tag{9.3}$$

The $\vartheta_{\rm III}$ is at the dipole equator on the boundary of the Szekeres region. One ray reaching Observer III will have $\vartheta=\pi/2$ throughout the Friedmann region.

The equations to be integrated are, from (5.7) – (5.11):

$$\frac{{\rm d}t}{{\rm d}\lambda} = k^t, \tag{9.4}$$

$$\frac{{\rm d}k^t}{{\rm d}\lambda} = -\frac{\mathcal{N}\mathcal{N}_{,t}}{1+2E}\left(k^r\right)^2-\frac{\Phi\Phi_{,t}}{\mathcal{F}^2}\left(k^\vartheta\right)^2, \tag{9.5}$$

$$\frac{{\rm d}\vartheta}{{\rm d}\lambda} = k^\vartheta, \tag{9.6}$$

$$\frac{{\rm d}k^\vartheta}{{\rm d}\lambda} = -2\frac{\Phi_{,t}}{\Phi}k^tk^\vartheta+\frac{\sin\vartheta S_{,r}\mathcal{N}}{S\Phi(1+2E)}\left(k^r\right)^2-2\frac{\mathcal{N}}{\Phi}k^rk^\vartheta + \frac{\sin\vartheta\left(S^2-{S_b}^2\right)}{2SS_b\mathcal{F}}\left(k^\vartheta\right)^2, \tag{9.7}$$

$$\frac{{\rm d}r}{{\rm d}\lambda} = k^r, \tag{9.8}$$

$$\xi \stackrel{\rm def}{=} \left(k^t\right)^2-\left(\frac{\Phi k^\vartheta}{\mathcal{F}}\right)^2, \tag{9.9}$$

$$k^r = \pm\frac{\sqrt{1+2E}}{\mathcal{N}}\sqrt{\xi}. \tag{9.10}$$

The initial values for (t,r,ϑ) will be at the observer positions specified above, the initial value for k^t is (5.12), and the rays will be calculated backward in time from there. With $k^\varphi=0$, Eq. (5.13) reduces to

$$\left(k^\vartheta_o\right)^2\le\left(\frac{\mathcal{F}_o}{\Phi_o}\right)^2. \tag{9.11}$$

As before, the equality occurs when $k^r_o = 0$.

When the observer is in the Friedmann region, $\mathcal{F}_o = 1$, as explained under Eq. (5.14). For Observer I Φ_o was calculated by the program that found (8.11); it is

$$(\Phi_o)_{\text{obs 1}} = 0.40173786327577615. \tag{9.12}$$

So, from (9.11), for Observer I

$$\left|\left(k^\vartheta_o\right)_{\max}\right| = 2.48918534052525. \tag{9.13}$$

Figure 3 shows that a past-directed ray emitted from Observer I position with $k^\vartheta_o = \left(k^\vartheta_o\right)_{\max}$ is indeed tangent to an r = constant hypersurface at its initial point. The coordinates in the figure are $X = -r\cos\vartheta$, $Y = r\sin\vartheta$. Images of rays in the figures are in general not straight because the spaces of constant t in the Friedmann background are not flat ($k \neq 0$ in (3.2)), so the figure planes are not their isometric images. The only null geodesics in the Friedmann region whose images in the figures are straight are those with ϑ = constant along them.

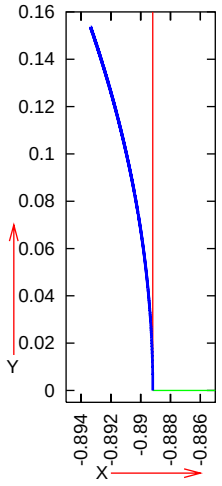

FIG. 3: The image of a ray that has $k^\vartheta_o = \left(k^\vartheta_o\right)_{\max}$ at Observer I. The straight lines show the directions of the X and Y axes. More explanation in the text.

The next figures show rays that stay over or near the BB hump for some of the flight time; their k^ϑ_o were found by trial and error. The initial value of k^r for each ray follows from (9.10) after the value of k^ϑ_o is chosen.

The step in λ was $\Delta\lambda = 10^{-9}$. At all initial points, $k^r < 0$, but ξ was monitored along each ray, and when it went down to or below zero, the sign of k^r was reversed.[6]

[6] $\xi < 0$ cannot happen on a null geodesic; see (5.11) with $k^\varphi = 0$. But in numerical calculations it happens because of numerical inaccuracy. If it happened at step n, then for this step ξ was replaced by $(-\xi)$, then it should begin to grow. However, in practice the sign reversals of ξ in a vicinity of the smallest r had to be done many times along some of the rays.

The angle α between two rays reaching an observer can be calculated as follows. The direction of a ray is determined by the unit spacelike vector given by [10]

$$n^\alpha = u^\alpha - \frac{k^\alpha}{k^\rho u_\rho}, \tag{9.14}$$

where k^α is the tangent vector to the ray and u^α is the velocity vector of the observer (comoving with the cosmic dust); $n^\alpha u_\alpha = 0$. Since $g_{\alpha\beta}n^\alpha n^\beta = -1$, the angle between two such directions, n^α_1 and n^α_2, is given by

$$\cos\alpha = g_{\alpha\beta}n^\alpha_1 n^\beta_2. \tag{9.15}$$

Since $u^\alpha = \delta^\alpha{}_0$ everywhere, and $k^0 = -1$ at the observer, the components of a general n^α at the observer are

$$n^\alpha_o = \left(0, k^r_o, k^\vartheta_o, k^\varphi_o\right). \tag{9.16}$$

Using (9.10), (5.3) and assuming $k^\varphi_o = 0$ we then obtain for the angle α_{RS} between rays R and S

$$\begin{aligned}\cos\alpha_{RS} &= \sqrt{1-\left(\frac{k^\vartheta_{Ro}\Phi_o}{\mathcal{F}_o}\right)^2}\times\sqrt{1-\left(\frac{k^\vartheta_{So}\Phi_o}{\mathcal{F}_o}\right)^2} \\ &+ k^\vartheta_{Ro}k^\vartheta_{So}\left(\frac{\Phi_o}{\mathcal{F}_o}\right)^2.\end{aligned} \tag{9.17}$$

Since both k^ϑ_o must obey (9.11), it follows that $|\cos\alpha_{AB}| \leq 1$, so (9.17) has a solution.

When ray R is axial ($k^\vartheta_{Ro} = 0$), and the observer lies in the Friedmann region where $\mathcal{F}_o = 1$, (9.17) becomes

$$\begin{aligned}\cos\alpha_{RS} &= \sqrt{1-\left(k^\vartheta_{So}\Phi_o\right)^2} \\ \Longrightarrow\quad \sin\alpha_{RS} &= k^\vartheta_{So}\Phi_o.\end{aligned} \tag{9.18}$$

This equation can be used to estimate the angular radius of a radiation source in the sky; then α is the angle between the direction of the central ray of the pencil (the one proceeding along the symmetry axis for observers I and II) and the direction of the ray that grazes the edge of the source. The latter can be approximately determined in numerical experiments.

The redshift in the Friedmann background between the LSH and the present time, calculated numerically along a null geodesic is

$$1 + z_b = 951.83531161489873. \tag{9.19}$$

This differs slightly from (4.6) that was calculated from the exact formula $1 + z^{\text{b}}_{\text{LS}} = \mathcal{R}_{\text{now}}/\mathcal{R}_{\text{LS}}$, where $\mathcal{R}$ is the Friedmann scale factor. It also differs from the $1 + z_{\text{comp}} = 951.91469714961829$ calculated for the same quantity in Ref. [1]. The differences are caused by numerical inaccuracies (in particular, a different numerical step was used in [1]). Since all null geodesics in the following will be calculated numerically, (9.19) will be taken as the reference value.

A. Rays reaching observer I

Table I lists the parameters of exemplary nonradial rays received by Observer I, with the angular radii calculated by (9.18). The angular radius of the whole BB hump (Ray 9 line in the table) is here somewhat smaller than the 1.00097° in the L–T/Friedmann model of Ref. [1]. Decreasing this radius was one of the aims of replacing the L–T region with Szekeres.

In Figs. 4 and 5 the coordinates are

$$X = -r\cos\vartheta, \qquad Y = r\sin\vartheta, \tag{9.20}$$

and the labels of the rays are the same as in the table. Figure 4 shows the projections of the rays from Table I in a vicinity of their end points on a surface of constant t along the flow lines of the dust.[7] Figure 5 is a closeup view on the neighbourhood of the BB hump in Fig. 4. The dotted circle is at $r = r_b$, the r-coordinate of the edge of the BB hump. The cross marks the center $r = 0$ of the dotted circle; the arrow on the horizontal arm of the cross in Fig. 5 points in the direction of the Szekeres dipole maximum. The large dots in Fig. 4 mark the points where the rays intersect the LSH. The end points of the rays are where the numerical calculation determined their crossing the BB. Figures 4 and 5 are nearly the same as the corresponding ones for the L–T/Friedmann model in Ref. [1]; there are only small quantitative differences between them. They are shown here to facilitate comparisons with the images of the rays reaching observers II and III further on.[8]

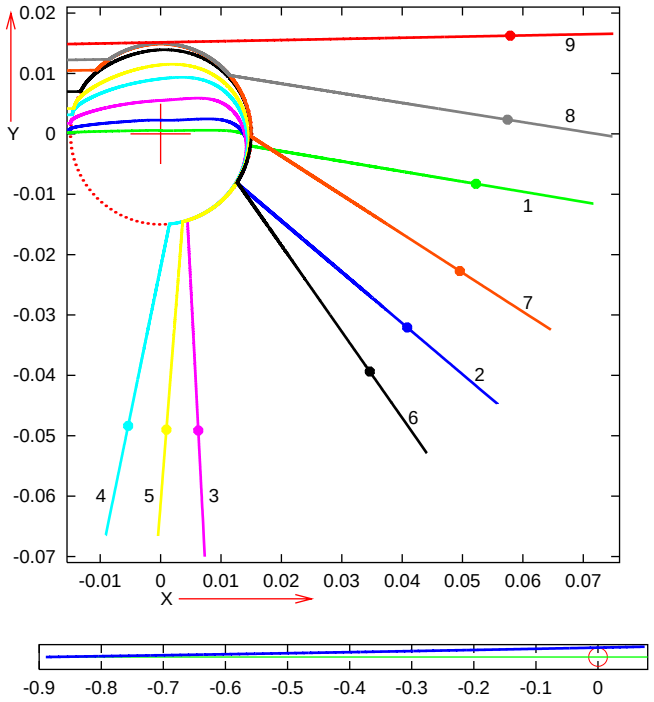

FIG. 4: **Upper panel:** Projections of the rays listed in Table I on a surface of constant t along the flow-lines of the cosmic dust. Observer I is at $X \approx -0.889, Y = 0$ beyond the left margin of the figure. The large dots mark the intersections of the rays with the last-scattering hypersurface. The dotted circle has the radius $r = A_1 + B_1$, where the BB hump has its edge. More explanation in the text. **Lower panel:** Ray 9 shown all the way between Observer I and the BB.

TABLE I: Parameters of nonaxial rays reaching Observer I

Ray	k_o^ϑ	ang. radius (°)	$1+z$ at LSH
0	0.000001	2.3×10^{-5}	368.90725567971225
1	0.0005	0.0115	379.24806292767818
2	0.002	0.046	379.39564761052731
3	0.005	0.115	458.61133144852778
4	0.009	0.207	613.97907545519695
5	0.012	0.276	728.81314339494827
6	0.02	0.460	909.33107425780156
7	0.03	0.691	971.73678884542733
8	0.035	0.806	959.84109447617345
9	0.0425	0.9783	951.84496752973837

Ray 0 is not included in the figures because, at their scale, it would coincide with the $Y = 0$ axis. It is included in the table in order to show how $1+z_{\rm LSH}$ abruptly jumps from the near-zero value (8.12) on an axial ray to a large positive value on a ray that is only slightly nonaxial.

The redshifts initially increase with the viewing angle. However, the maximum in $z_{\rm LSH}$ is achieved inside the image of the source, not at its edge, and it is larger than the background (9.19) – see Rays 7 and 8 in Table I. The same thing happened in the L–T/Friedmann model [1], and will again occur for Observers II and III further in this paper. Ray 9 is the one that just grazes the world-tube $r = r_b$, and $z_{\rm LSH}$ on it is close to (9.19).

The rays abruptly change their direction every time they come near to the surface $r = r_b$. The change is sharper when the ray is closer to the BB on its second intersection with $r = r_b$. When the rays travel over the BB hump further from its edge the deflections are smaller.

The angle of deflection of a ray depends on the interval of t that the ray spends near the edge of the BB hump. Ray 1 meets $r = r_b$ nearly head-on and does not strongly change direction on first encounter, when it is higher above the BB. However, on second encounter, it is closer to the BB and is forced to bend around more.

The other rays meet the $r = r_b$ surface at smaller an-

[7] In comoving coordinates, the projections do not depend on t.

[8] In Figs. 4 – 8 the circles of constant r in the Szekeres region would all be concentric with the dotted circle. To demonstrate their non-concentricity in the spaces of constant t, one should calculate their geodesic radii and geodesic distances between them. The resulting image would be similar to Fig. 1 in Ref. [2].

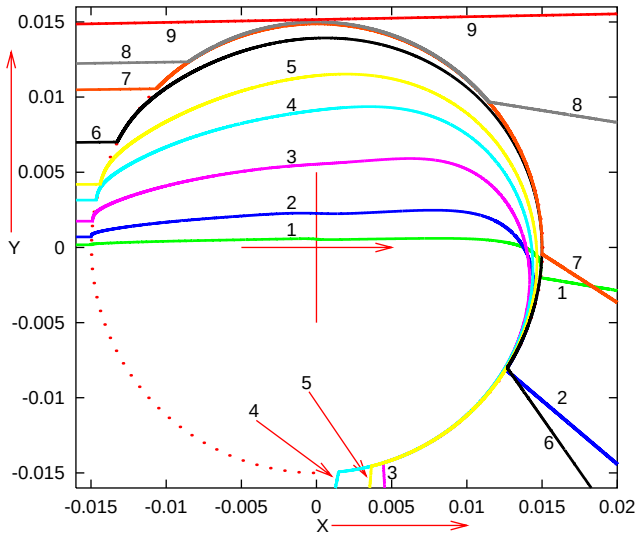

FIG. 5: The region near the BB hump in Fig. 4. The arrow on the horizontal arm of the cross points in the direction of the dipole maximum. More explanation in the text.

gles than ray 1, so they stay near that surface for longer times. For rays 3, 4 and 5 this gives the effect that they are deflected much stronger than ray 1. For ray 6 and the other ones, a different effect prevails: they fly farther from the BB, so approach the BB later and stay within its influence for a shorter time, therefore the deflection angle decreases again. Ray 9 does not enter the Szekeres region but only touches it, so it propagates almost undisturbed as in the Friedmann region.

Figures 4 and 5 show only those rays for which $k_o^\vartheta > 0$. The images of the rays with $k_o^\vartheta < 0$ are mirror-reflections of those shown. In fact, since $\vartheta = 0$ is the axis of symmetry, the image will be the same for every φ, so one should imagine the complete collection of constant-φ null geodesics by rotating Fig. 4 around the $\vartheta = 0$ axis.

B. Rays reaching Observer II

Table II and Fig. 6 calculated for Observer II are analogues of Table I and Fig. 5. The analogue of ray n from Table I is ray $10+n$ in Table II. The k_o^ϑ are the same as in Table I, with the exception of Ray 19 – see below for an explanation. The angular radii are slightly larger here because Φ_o for Observer II is slightly larger than (9.12):

$$(\Phi_o)_{\text{obs 2}} = 0.40181424093371831. \tag{9.21}$$

This is because $\widetilde{r}_{\text{obs}}$ of (8.19) is larger than r_{obs} of (8.13). But at the level of precision used in the tables, the angular radii for Rays 11 – 18 are the same as those for Rays 1 – 8. The analogue of Ray 0 is not included.

Ray 19 grazes the edge of the Szekeres region – so its k_0^ϑ determines the angular radius of the whole source by (9.18). Since r_{obs} is larger here, the k_o^ϑ for Ray 19 had to be determined anew, and it is smaller than for Ray 9. The angular radius of the source seen by Observer II is

$$\alpha_{\text{II}} = 0.9681^\circ. \tag{9.22}$$

TABLE II: Parameters of rays reaching Observer II

Ray	k_o^ϑ	$1+z$ at LSH
11	0.0005	358.22989174485627
12	0.002	388.80853980783820
13	0.005	408.06476517495747
14	0.009	504.79183448874682
15	0.012	620.08511872418046
16	0.02	885.02972357472424
17	0.03	970.70644144723383
18	0.035	982.13817446295479
19	0.04205	951.83804564661989

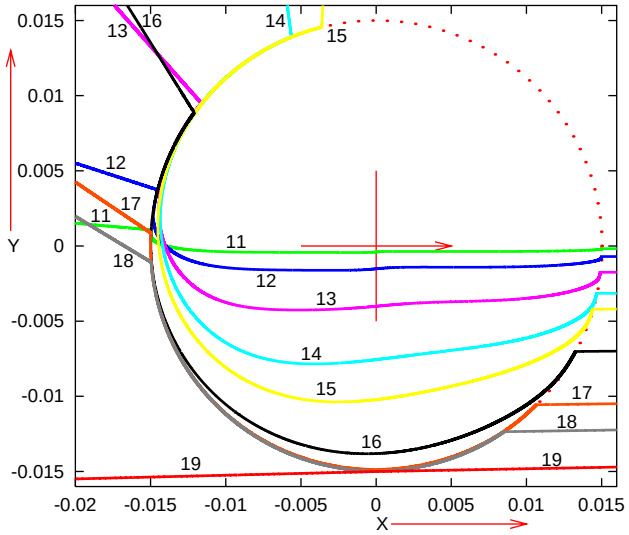

FIG. 6: The analogue of Fig. 5 for Observer II, who is at $X \approx 0.889, Y = 0$ beyond the right margin of the figure. See Table II for the parameters of the rays.

The values of $1+z_{\text{LSH}}$ in Table II are different from the corresponding ones in Table I, but the general pattern is the same: the redshift initially increases with the viewing angle, achieves a maximum inside the image of the source, then decreases to the background value at the edge of the image. The maximum is achieved here at a larger k_o^ϑ, on Ray 18, while it occurred on Ray 7 for Observer I. When the detectors achieve a sufficient precision to resolve the images of the GRBs (which now appear as fuzzy dots of angular radius $\approx 0.5^\circ$ [7]), it will become possible to compare the patterns of $1+z_{\text{LSH}}$ across the images with observations. Thereby it will be possible to test and modify the parameters of models.

C. Rays reaching observer III

Observer III, unlike Observers I and II, is not located on the axis of symmetry, so the (past-directed) rays going off from her position with $k_o^\vartheta < 0$ will not be mirror-images of those with $k_o^\vartheta > 0$. Therefore, these two groups of rays are shown in separate tables and separate figures. Table III and Fig. 7 contain the rays for which $k_o^\vartheta \leq 0$; the rays in Table IV and Fig. 8 have $k_o^\vartheta > 0$. The set of values of $\left|k_o^\vartheta\right|$ is the same as in Table I and Fig. 5. The analogues of ray n from Table I are ray $20+n$ in Table III and ray $30+n$ in Table IV.

TABLE III: Parameters of rays with $k_o^\vartheta \leq 0$ at Observer III

Ray	k_o^ϑ	$1+z$ at LSH
20	0.0	390.14254818860690
21	-0.0005	389.38105384339815
22	-0.002	383.44315068756219
23	-0.005	403.96885207547047
24	-0.009	518.01433335656031
25	-0.012	657.82355530702455
26	-0.02	901.00572735399282
27	-0.03	957.37762498857785
28	-0.035	981.74423314432147
29	-0.0425	951.84597923424201

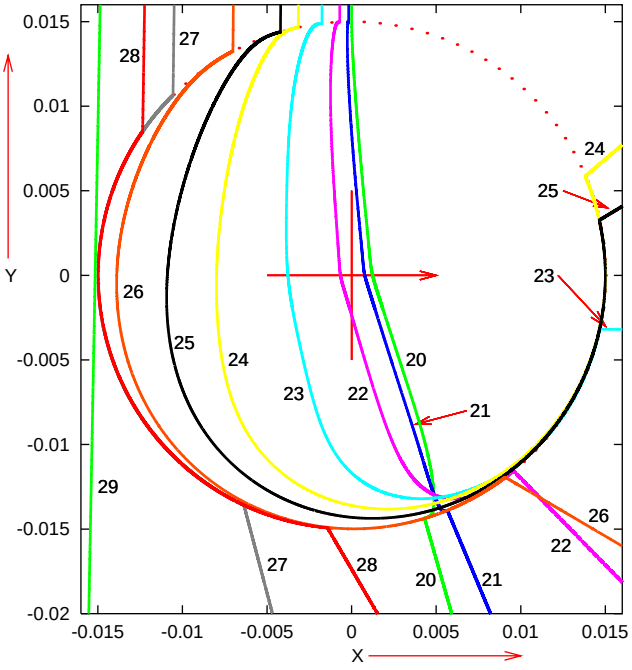

FIG. 7: The analogue of Fig. 5 for Observer III, who is at $X=0, Y\approx 0.889$ above the upper edge of the figure. This figure shows only those rays that have $k_o^\vartheta \leq 0$; see Table III for their parameters.

The value of Φ_o is here between the previous ones,

$$(\Phi_o)_{\text{obs 3}} = 0.40177605010003492, \tag{9.23}$$

while $t_o = 0$ does not differ significantly from (8.20) and (8.21), so the angular radii would also be intermediate; they are not listed in the tables.

The most conspicuous difference from the previous cases is in Ray 20 that proceeds along $\vartheta = \pi/2$ in the Friedmann region: it is deflected toward larger ϑ on entry to the Szekeres region, and bends oppositely to all other rays on leaving it. Rays 21 and 22 get deflected so strongly that they cross the line $\vartheta = \pi/2, 3\pi/2$ well inside the Szekeres region, unlike their analogues, Rays 1, 2, 11 and 12, which cross the $\vartheta = 0, \pi$ lines just before leaving the Szekeres region. Beginning with Ray 23, the paths of the rays become similar (though different in numerical detail) to the corresponding ones for Observers I and II.

For rays with $k_o^\vartheta < 0$ the pattern of $1+z_{\text{LSH}}$ across the image of the source is different from those for Observers I and II: with decreasing $k_o^\vartheta < 0$ the redshift first decreases to a minimum on Ray 22, then increases to a maximum larger than in the background on Ray 28, and then drops to the background value. In this family of rays there is one that will pass through $r = 0$, but with $0 < \vartheta < \pi$, so it will not have $z = -1$ at the BB for the reason indicated under Eq. (6.4). See also Ref. [2], where rays passing through $r = 0$ were numerically integrated for the same kind of Szekeres dipole (but with a different BB profile and with $a^2 = 0.1$) – only those proceeding along $\vartheta = 0$ or $\vartheta = \pi$ had $z \approx -1$ near the BB.

TABLE IV: Parameters of rays with $k_o^\vartheta > 0$ at Observer III

Ray	k_o^ϑ	$1+z$ at LSH
31	0.0005	400.78949750617528
32	0.002	420.91096504818154
33	0.005	484.00268387494344
34	0.009	598.89267241083019
35	0.012	698.93002088862590
36	0.02	895.36511128123175
37	0.03	957.37820413798283
38	0.035	981.62140475009016
39	0.0425	951.84597923424201

For rays with $k_o^\vartheta > 0$ the pattern of $1+z_{\text{LSH}}$ is similar to that for Observer II: there is only the maximum, achieved on Ray 38. However, most values of $1+z_{\text{LSH}}$ differ substantially from their counterparts in Table II.

The paths of the rays are similar to those for Observers I and II, but the angle of deflection is smaller for each ray here. Also, the rays bend away from the $X = 0$ axis near the $Y = 0$ line – this effect was not visible for Observer I and barely noticeable for Observer II.

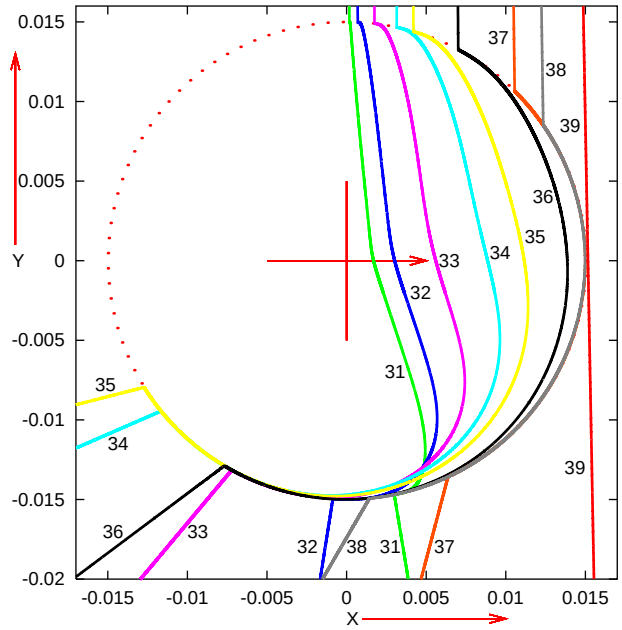

FIG. 8: The rays that have $k_o^\vartheta > 0$ at Observer III; see Table IV for their parameters.

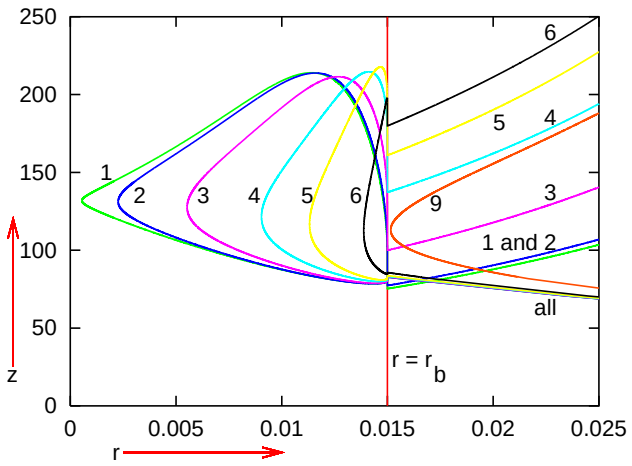

FIG. 10: The $z(r)$ relations for some rays from Fig. 4. Along rays 1 – 6 z has two maxima and two minima, which points to the existence of an analogue of the Extremum Redshift Surface along them. Ray 9 does not enter the blueshift-generating region, so z is increasing all along it.

X. REDSHIFT PROFILES ALONG NONAXIAL NULL GEODESICS

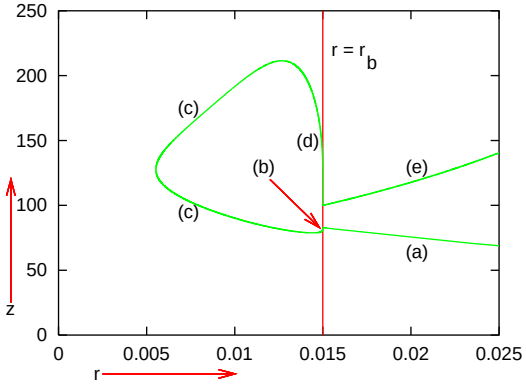

FIG. 9: The $z(r)$ relation for Ray 3 from Fig. 4 and its characteristic branches. Observer I is at $r \approx 0.889$ beyond the right edge of this figure. See text for explanation.

The z-profiles along rays 1 – 9 are shown in Fig. 9 and 10; they are similar to those in the L–T/Friedmann model [1]. They prove that analogues of the ERS (call them ERS') exist also along nonaxial rays. Figure 9 shows the $z(r)$ relation for Ray 3 in a neighbourhood of $r = r_b$; it serves as a key to reading Fig. 10. In Fig. 9, in segment (a) of the ray, z increases from 0 at the observer to a local maximum at $r \approx r_b$, where the (past-directed) ray intersects the outer branch of the ERS' for the first time. Then, in segment (b), z decreases to a local minimum at a slightly smaller r, where the ray intersects the inner branch of the ERS' for the first time. Further along the ray, in segment (c), z increases until it reaches the second local maximum at the second intersection of the ray with the inner branch of the ERS'. Then, in segment (d), z decreases up to the second intersection of the ray with the outer branch of the ERS', where it achieves its second and last local minimum. From then on, in segment (e), z keeps increasing up to ∞ achieved at the BB.

Along some other rays in Fig. 10, the second minimum of z is smaller than the first maximum, so those $z(r)$ curves self-intersect.

XI. FITTING THE GRB SOURCES IN THE CELESTIAL SPHERE

Imagine a GRB source to be a disk on the celestial sphere of angular radius ϑ_0. How many such sources would fit into the celestial sphere at the same time?

An equivalent question is: how many non-overlapping circles of a given radius can be drawn on a sphere of a given radius. A rough answer would be obtained by dividing the surface area of the sphere by the surface area inside the circle. But this would be an overestimate – the circles cannot cover the sphere completely. A more realistic approximation is to imagine each circle being inscribed into a quadrangle of arcs of great circles on the sphere. Such figures cannot cover the sphere, either, but this method takes into account some of the area outside the circles, and it yields an upper bound on the number we wish to know. Details of the calculation are presented in the Appendix. It turns out that the area of the sphere divided by the area of such a quadrangle is

$$\mathcal{N} = \frac{\pi}{\arcsin\left(\sin^2\vartheta_0\right)}. \qquad (11.1)$$

Taking $\vartheta_0 = 0.5°$, which is the current resolution of the GRB detectors [7], we obtain

$$\mathcal{N}_{0.5} \approx 41,254. \tag{11.2}$$

It would take that many GRB sources to cover the whole sky if their angular radii were indeed 0.5°. With $\vartheta_0 = 0.9783°$, as in the last line of Table I, we obtain

$$\mathcal{N}_{0.9783} \approx 10,776. \tag{11.3}$$

Finally, with $\vartheta_0 = 0.9681°$, as in (9.22), we obtain

$$\mathcal{N}_{0.9783} \approx 11,005. \tag{11.4}$$

These numbers should be compared with the number of GRBs actually detected in observations. This author was not able to get access to a definitive answer, but here is an estimate based on partial information. The BATSE (Burst and Transient Source Explorer) detectors, which are supposed to be the most sensitive existing, during the first 9 years of their operation, discovered 2704 GRBs [29]. Since they were first launched in 1991 [30], they have had so far the chance to work for 27 years. Assuming the same rate of new discoveries, they should have detected 8112 GRBs until now – still fewer than (11.4).

In order to decrease the angular radii cited in (11.3) and (11.4), the profile of the BB hump and the Szekeres functions P, Q and S should be further refined. When the angular radius is divided by the factor f, the number of possible GRB sources in the sky is multiplied by f^2. (This is intuitively obvious, and (11.1) approximately confirms this, since for small ϑ_0 we have $\sin\vartheta_0 \approx \vartheta_0 \approx \arcsin\vartheta_0$.)

XII. POSSIBLE IMPROVEMENTS OF THE MODEL

The model presented here needs improvements to be brought into quantitative agreement with the current GRB observations. It accounts for the lowest frequency of the radiation in the observed GRBs (the model of highest-frequency GRBs was discussed in Ref. [1]). Its main problem is that the angular radius of the radiation sources seen by the present observer is twice as large as the current observations allow (nearly 1° in the model vs. 0.5° – the limit of resolution of the GRB detectors [7]). In order to decrease this angle, the BB hump that emits the gamma rays should be made narrower or lower; in the second case it would be further away from the observer during the gamma-ray flash. The BB profile chosen in this paper is not yet the limit of improvement. The first, rather rough, attempt to explain the GRBs using a cosmological blueshift resulted in a model [31] whose hump had the height $A_0 + B_0 = 0.026$ NTU and width $A_1 + B_1 = 0.108$. By experimenting with the parameters of the hump (including the degree of the equation in (3.5)), the numbers in (3.8) were achieved, i.e. the height was decreased ≈ 206 times, and the width 7.2 times. A further improvement was tried in Sec. VIII here, but it gave a rather modest result.

To get small $1 + z$ the BB profile should be such that the blueshifted ray spends as much time as possible traveling above the LSH but still below the ERS. As follows from (7.7) and (7.8), the room under the ERS becomes larger when $\mathrm{d}t_B/\mathrm{d}r$ is larger and when a is smaller. The problem with small a was described in Sec. VIII, but it might be overcome using a greater numerical precision. A larger $\mathrm{d}t_B/\mathrm{d}r$ causes the BB hump to become higher. In order to keep the hump height acceptably small, the large $\mathrm{d}t_B/\mathrm{d}r$ has to be limited to a short interval of r – this is where the steep slope of the hump in Fig. 2 came from. The field is open for further optimization. For example, in this paper the function $E(r)$ had the Friedmann shape (3.2) throughout the Szekeres region – obviously it should be checked what happens when it has non-Friedmannian shapes. Other Friedmann backgrounds than the one of Sec. IV should be tested. Other Szekeres dipoles than (3.9) should also be tested, in particular nonsymmetric ones. Carrying out such tests is laborious – it involves finding, by numerical shooting, the minimum of a function of several variables (in this paper these were 7 variables: the five in (3.8), the a of (3.9) and the Δt_c of (8.4)).

Similar to the L–T model of Ref. [1], the model presented here implies too long durations for the GRBs and for their afterglows. This is because, in axially symmetric models, once the observer and the source are placed on the symmetry axis, they stay there forever – the source does not drift [13]. The only changes of the observed frequency and intensity may occur because the observer receives rays emitted from different points of the BB hump along the same line of sight, so the changes occur on the cosmological time scale and are much slower than observed (see Ref. [1] for the numbers).

A nonsymmetric Szekeres model offers a new possibility. As shown in Ref. [2], in such a model there also exist two opposite directions along which radiation is strongly blueshifted. However, the effect of non-repeatability of the light paths [13] (also called 'cosmic parallax' [14]) will cause that an observer who was initially in the path of one of those preferred rays will get off it after a while. The time-scale of this process still needs to be calculated, but it is rather clear that it should be short in consequence of the very large distance between the source and the observer and of the discontinuous change from blueshift to redshift as soon as the observer gets off the magic line.

XIII. SUMMARY AND CONCLUSIONS

In Ref. [2], existence and properties of blueshifts in exemplary simple quasi-spherical Szekeres models were investigated. Using that knowledge, in the present paper it was investigated whether a QSS mass-dipole superposed on an L–T background would allow modeling gamma-ray

bursts by cosmological blueshifting more precise than in Ref. [1], where pure L–T models were used. The axially symmetric QSS model was introduced in Secs. II and III. This QSS region is embedded in a negative-spatial-curvature Friedmann background (Sec. IV), chosen for correspondence with earlier papers by this author [19, 20]. After presenting preliminary definitions and information in Secs. V, VI and VII (mostly repeated after Ref. [2]), in Sec. VIII the parameters of the QSS model are chosen such that at present the highest frequency of the blueshifted radiation agrees with the lowest frequency of the observed GRBs (this agreement requires that the blueshift between the last scattering and the present time obeys $1 + z \leq 1.689 \times 10^{-5}$ [1]). The introduction of the Szekeres dipole has the consequence that the required $1 + z$ is achieved with a lower hump in the BB profile, so at a greater distance between the radiation source and the observer than in the L–T model. In Sec. IX, the paths of nonaxial light rays reaching three different present observers are presented. The observers are placed in prolongation of the mass-dipole maximum axis, of the dipole minimum axis, and of the dipole equator. The distributions of the observed redshift *across* the image of the source are different for each observer, and the angular radii of the source are found to be between $0.9681°$ and $0.9783°$. This is nearly twice as much as the current GRB observations allow, but the model has the potential to be improved (see Sec. XII). In Sec. X, the redshift profiles *along* nonaxial rays were calculated in order to show that extrema of redshift exist also along them. In Sec. XI it was estimated that with the angular radii of the GRB sources being between $0.9681°$ and $0.9783°$, approximately 11,000 such sources could be simultaneously fitted into the sky of the present observer; this is to be compared with $\approx 8,100$ GRBs that had a chance to be seen by the BATSE detectors [29] since 1991. Finally, possible further improvements in the model were discussed in Sec. XII.

The models of generating the GRBs discussed here and in Ref. [1] are subject to two kinds of tests:

1. In the future, when the instrumental precision improves, the observers should be able to resolve the fuzzy disks they now see as GRB sources [7], and measure the distribution of radiation frequencies and intensities across them. Then it will be possible to compare those distributions with model predictions. A model that would predict such a distribution correctly could then be used to get information about the sources.

2. If gamma radiation is generated simultaneously with the CMB radiation, as proposed in Ref. [1] and in the present paper, then it is observed now as a short-lived flash because its source comes into and out of the observer's view, but has existed there since the last scattering epoch. In this case, the central gamma-ray should be surrounded by rays with positive redshifts smoothly blending with the CMB background at the edge of the source image, as shown in tables in Sec. IX. But if a source of a GRB lies later than the last scattering, then it is independent of the CMB. It should black out all CMB rays within some angle around the central gamma ray, and the blackout should continue even after the gamma-ray flash is over. The redshift distribution across the image of the source would have no reason to continuously match the CMB at the edge.

This author does not wish to question the validity of the GRB models proposed so far. The basic motivation was this: history of science teaches us that if a well-tested theory predicts a phenomenon, then the prediction has to be taken seriously and checked against experiments and observations. Since general relativity clearly predicts that some of the light generated during last scattering should reach us with strong blueshift, consequences of this prediction have to be worked out and submitted to tests – especially in view of the fact that models with nonconstant $t_B(r)$ that are capable of generating blueshifts are *generic*. It is the Robertson – Walker class of models that is highly exceptional in several respects. To give just three examples: (1) They have unusually high symmetry that trivializes the whole wealth of geometries allowed by Einstein's equations to a two-parameter family of solutions of one ordinary differential equation. (2) They are the only ones in which the spatial curvature is constant in all of space (according to the inflationary propaganda this curvature should be exactly zero). In L–T and Szekeres models the spatial curvature at any time varies with position. (3) They are the only ones in a large class in which the cosmic drift is zero on all null geodesics [13, 32, 33]. The possible existence of this effect would have never been predicted if more general models were not investigated.

To quote from Ref. [19]: "We generally agree that Nature acts through mathematics. If so, then it is reasonable to assume that it takes the tools from a generic set, e.g., not a constant function when nonconstant ones are admissible, not a function of 2 variables when 3 are possible, etc." Why should Nature ignore all these freedoms in constructing the Universe?

Appendix A: How many circles of a given radius can be drawn on a sphere of a given radius?

Imagine a circle K drawn on a sphere S of radius a and a cone that intersects S along K and has its vertex at the center of S; see Figs. 11 and 12. Let the opening angle of the cone be ϑ_0. Now imagine a square pyramid circumscribed on this cone. The pyramid intersects S along the curvilinear quadrangle shown in thicker lines in Fig. 11. The part of S inside the quadrangle has the surface area eight times the surface area inside the curvilinear triangle ABC; see also Fig. 13.

Suppose the center of the sphere is at $x = y = z = 0$, so the equation of the sphere is $x^2 + y^2 + z^2 = a^2$, and the axis of the cone goes along the z axis. The metric of

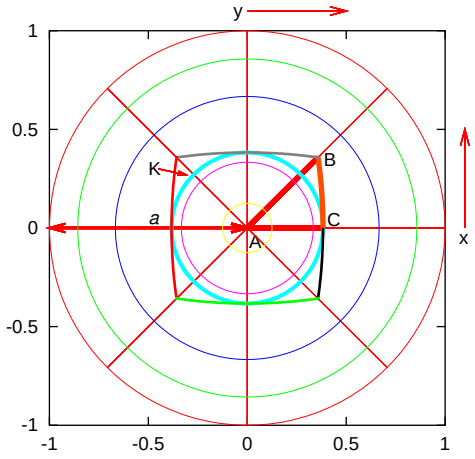

FIG. 11: View from the $z > 0$ axis on the cone and the pyramid. They intersect the sphere along the circle K and the curvilinear quadrangle shown in thicker lines, respectively. The surface area inside this quadrangle is eight times the surface area inside the curvilinear triangle ABC.

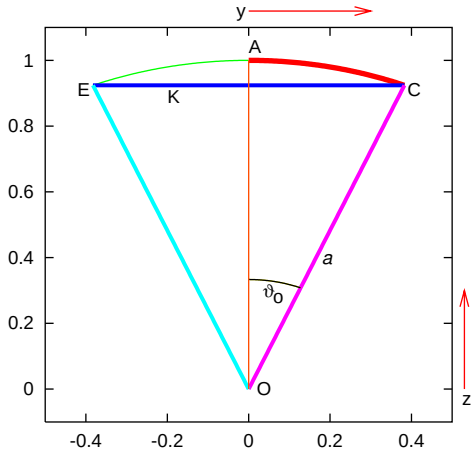

FIG. 12: Projection of the cone and of the pyramid from Fig. 11 on the $x = 0$ coordinate plane. The lines OE and OC are intersections of the cone (and of the faces of the pyramid) with the plane of the figure; the letters K, A and C have the same meaning as in Fig. 11.

the sphere in the (x, y) coordinates is

$$\mathrm{d}x^2 + \mathrm{d}y^2 + \mathrm{d}z^2 = \frac{\left(a^2 - y^2\right)\mathrm{d}x^2 + 2xy\mathrm{d}x\mathrm{d}y + \left(a^2 - x^2\right)\mathrm{d}y^2}{a^2 - x^2 - y^2}, \tag{A1}$$

and so the surface element of the sphere is

$$\sqrt{g}\mathrm{d}x\mathrm{d}y = \frac{a}{\sqrt{a^2 - x^2 - y^2}}\mathrm{d}x\mathrm{d}y. \tag{A2}$$

The side AC of the triangle lies in the plane $x = 0$, and y on it changes from 0 to $a \sin\vartheta_0$. The side AB lies in the plane $y = x$. The y-coordinate of the point B is

$$y_\mathrm{B} = \frac{a \sin\vartheta_0}{\sqrt{1 + \sin^2\vartheta_0}}, \tag{A3}$$

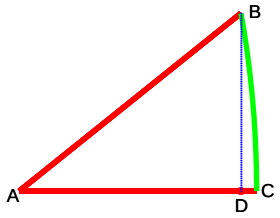

FIG. 13: An auxiliary sketch to calculate the surface area of the triangle ABC on a sphere. See text.

as is easy to calculate knowing that this point lies simultaneously on the sphere $x^2 + y^2 + z^2 = a^2$, in the plane $y = x$ and in the plane $z = y \cot\vartheta_0$ that contains the right face of the pyramid. The auxiliary point D has the same y-coordinate as B. The arc BC (which is part of the intersection of the right face of the pyramid with the sphere) obeys the equation

$$x = \sqrt{a^2 - \frac{y^2}{\sin^2\vartheta_0}} \stackrel{\mathrm{def}}{=} x_\mathrm{BC}(y). \tag{A4}$$

The surface area of the triangle ABC is thus

$$\begin{aligned} S_\mathrm{ABC} &= \int_0^{y_\mathrm{B}} \mathrm{d}y \int_0^{y} \frac{a}{\sqrt{a^2 - x^2 - y^2}}\,\mathrm{d}x \\ &+ \int_{y_\mathrm{B}}^{a\sin\vartheta_0} \mathrm{d}y \int_0^{x_\mathrm{BC}(y)} \frac{a}{\sqrt{a^2 - x^2 - y^2}}\,\mathrm{d}x \qquad \text{(A5)} \\ &= \int_0^{y_\mathrm{B}} a \arcsin\left(\frac{y}{\sqrt{a^2 - y^2}}\right)\mathrm{d}y \\ &+ \int_{y_\mathrm{B}}^{a\sin\vartheta_0} a \arcsin\left(\frac{x_\mathrm{BC}(y)}{\sqrt{a^2 - y^2}}\right)\mathrm{d}y. \qquad \text{(A6)} \end{aligned}$$

The two integrals in (A6) are

$$S_I = \frac{a^2\vartheta_0 \sin\vartheta_0}{\sqrt{1 + \sin^2\vartheta_0}} - \tfrac{1}{2}\, a^2 \arcsin\left(\sin^2\vartheta_0\right), \tag{A7}$$

$$S_{II} = -\frac{a^2\vartheta_0 \sin\vartheta_0}{\sqrt{1 + \sin^2\vartheta_0}} + a^2 \arcsin\left(\sin^2\vartheta_0\right). \tag{A8}$$

So, the area of the triangle ABC is $\frac{1}{2}\, a^2 \arcsin\left(\sin^2\vartheta_0\right)$, and the area of the quadrangle in Fig. 11 is

$$S_\mathrm{quad} = 4a^2 \arcsin\left(\sin^2\vartheta_0\right). \tag{A9}$$

(When $\vartheta_0 = \pi/2$, this gives the obvious result $2\pi a^2$.)

Hints for the less-trivial parts of calculating the integrals:

In S_I change the variables by $\arcsin\left(\frac{y}{\sqrt{a^2-y^2}}\right) = w$ and integrate by parts to get rid of the factor w under the integral.

In S_{II} change the variables by $y = a \sin\vartheta_0 \sin u$, then integrate by parts to get rid of arcsin under the integral, and finally use the identity $\arctan\lambda = \arcsin\left(\frac{\lambda}{\sqrt{1+\lambda^2}}\right)$.

Now an approximate answer to the question in the title can be given. The quadrangles will not cover the whole surface of the sphere, but by dividing the surface area of the sphere, $4\pi a^2$, by $S_{\rm quad}$ we obtain an upper bound on the number of nonoverlapping circles that can be drawn on the sphere; it is (11.1).

Acknowledgement In deriving the geodesic equations, the computer-algebra system Ortocartan [34, 35] was used. The statement quoted at the end of Sec. XIII emerged from discussions with Michał Szurek.

[1] A. Krasiński, Cosmological blueshifting may explain the gamma ray bursts. *Phys. Rev.* **D93**, 043525 (2016).

[2] A. Krasiński, Existence of blueshifts in quasi-spherical Szekeres spacetimes. *Phys. Rev.* **D94**, 023515 (2016).

[3] G. Lemaître, L'Univers en expansion [The expanding Universe]. *Ann. Soc. Sci. Bruxelles* **A53**, 51 (1933); English translation: *Gen. Relativ. Gravit.* **29**, 641 (1997); with an editorial note by A. Krasiński: *Gen. Relativ. Gravit.* **29**, 637 (1997).

[4] R. C. Tolman, Effect of inhomogeneity on cosmological models. *Proc. Nat. Acad. Sci. USA* **20**, 169 (1934); reprinted: *Gen. Relativ. Gravit.* **29**, 935 (1997); with an editorial note by A. Krasiński, in: *Gen. Relativ. Gravit.* **29**, 931 (1997).

[5] P. Szekeres, Naked singularities. In: *Gravitational Radiation, Collapsed Objects and Exact Solutions*. Edited by C. Edwards. Springer (Lecture Notes in Physics, vol. 124), New York, pp. 477 – 487 (1980).

[6] C. Hellaby and K. Lake, The redshift structure of the Big Bang in inhomogeneous cosmological models. I. Spherical dust solutions. *Astrophys. J.* **282**, 1 (1984) + erratum *Astrophys. J.* **294**, 702 (1985).

[7] Private communication in 2015 from Linda Sparke, then at NASA.

[8] P. Szekeres, A class of inhomogeneous cosmological models. *Commun. Math. Phys.* **41**, 55 (1975).

[9] P. Szekeres, Quasispherical gravitational collapse. *Phys. Rev.* **D12**, 2941 (1975).

[10] J. Plebański and A. Krasiński, *An Introduction to General Relativity and Cosmology*. Cambridge University Press 2006, 534 pp, ISBN 0-521-85623-X.

[11] Planck collaboration, Planck 2013 results. XVI. Cosmological parameters. *Astron. Astrophys.* **571**, A16 (2014).

[12] Planck collaboration, Planck 2013 results. XV. CMB power spectra and likelihood. *Astron. Astrophys.* **571**, A15 (2014).

[13] A. Krasiński and K. Bolejko, Redshift propagation equations in the $\beta' \neq 0$ Szekeres models. *Phys. Rev.* **D83**, 083503 (2011).

[14] C. Quercellini, L. Amendola, A. Balbi, P. Cabella, M. Quartin, Real-time cosmology. *Phys. Rep.* **521**, 95 – 134 (2012).

[15] C. Hellaby, The nonsimultaneous nature of the Schwarzschild $R = 0$ singularity. *J. Math. Phys.* **37**, 2892 (1996).

[16] W. B. Bonnor, A. H. Sulaiman and N. Tomimura, Szekeres's space-times have no Killing vectors, *Gen. Rel. Grav.* **8**, 49 (1977).

[17] M. M. de Souza, Hidden symmetries of Szekeres quasispherical solutions, *Revista Brasileira de Física* **15**, 379 (1985).

[18] C. Hellaby and A. Krasiński. You cannot get through Szekeres wormholes or regularity, topology and causality in quasi-spherical Szekeres models. *Phys. Rev.* **D66**, 084011 (2002).

[19] A. Krasiński, Blueshifts in the Lemaître – Tolman models. *Phys. Rev.* **D90**, 103525 (2014).

[20] A. Krasiński, Accelerating expansion or inhomogeneity? A comparison of the ΛCDM and Lemaître – Tolman models. *Phys. Rev.* **D89**, 023520 (2014) + erratum *Phys. Rev.* **D89**, 089901(E) (2014).

[21] Energy and Work Units Conversion, http://www.asknumbers.com/EnergyWorkConversion.aspx

[22] P. J. E. Peebles, Recombination of the Primeval Plasma, *Astrophys. J.* **153**, (1968).

[23] Ya. B. Zeldovich, V. G. Kurt, R. A. Syunyaev, Recombination of hydrogen in the hot model of the Universe, *Zhurn. Eksper. Teor. Fiz.* **55**, 278 (1968).

[24] Recombination (cosmology), https://en.wikipedia.org/wiki/Recombination_(cosmology)

[25] K. Bolejko, A. Krasiński, C. Hellaby and M.-N. Célérier, Structures in the Universe by exact methods – formation, evolution, interactions. Cambridge University Press 2010, 242 pp, ISBN 978-0-521-76914-3.

[26] B. C. Nolan and U. Debnath, Is the shell-focusing singularity of Szekeres space-time visible? *Phys. Rev.* **D76**, 104046 (2007).

[27] G. F. R. Ellis, Relativistic cosmology. In *Proceedings of the International School of Physics "Enrico Fermi", Course 47: General relativity and cosmology*. Edited by R.K. Sachs, Academic Press, 1971, pp. 104-182. Reprinted: *Gen. Relativ. Gravit.* **41**, 581 (2009); with an editorial note by W. Stoeger, in *Gen. Relativ. Gravit.* **41**, 575 (2009).

[28] A. Krasiński, C. Hellaby, K. Bolejko and M.-N. Célérier, Imitating accelerated expansion of the Universe by matter inhomogeneities – corrections of some misunderstandings. *Gen. Rel. Grav.* **42**, 2453 (2010).

[29] BATSE All-Sky Plot of Gamma-Ray Burst Locations, https://heasarc.gsfc.nasa.gov/docs/cgro/cgro/batse_src.html

[30] Gamma-ray burst, https://en.wikipedia.org/wiki/Gamma-ray_burst

[31] A. Krasiński, Gamma ray bursts may be blueshifted bundles of the relic radiation. arXiv:1502.00506, unpublished.

[32] A. Krasiński, Repeatable light paths in the shearfree normal cosmological models. *Phys. Rev.* **D84**, 023510 (2011).

[33] A. Krasiński, Repeatable light paths in the conformally flat cosmological models. *Phys. Rev.* **D86**, 064001 (2012).

[34] A. Krasiński, The newest release of the Ortocartan set of programs for algebraic calculations in relativity. *Gen. Relativ. Gravit.* **33**, 145 (2001).

[35] A. Krasiński, M. Perkowski, *The system ORTOCARTAN – user's manual*. Fifth edition, Warsaw 2000.